




# Correlation between spin–phonon coupling and magneto-electric effects in CoFe<sub>2</sub>O<sub>4</sub>/PMN-PT nanocomposite: Raman spectroscopy and XMCD study

Anju Ahlawat<sup>1,2,\*</sup> , Azam Ali Khan<sup>1,3</sup>, Pratik Deshmukh<sup>1,3</sup>, Mandar M. Shirolkar<sup>4</sup>, A. K. Sinha<sup>5</sup>, S. Satapathy<sup>1,3</sup>, V.G.Sathe<sup>2</sup>, and R. J. Choudhary<sup>2</sup>

<sup>1</sup>Laser and Functional Materials Division, Ra Ja Ramanna Centre for Advanced Technology, Indore 452013, India

<sup>2</sup>UGC DAE Consortium for Scientific Research, Indore 452001, India

<sup>3</sup>Homi Bhabha National Institute, Training School Complex, Anushakti Nagar, Mumbai 400094, India

<sup>4</sup>Symbiosis Center for Nanoscience and Nanotechnology (SCNN), Symbiosis International (Deemed University) (SIU), Lavale, Pune, Maharashtra 412115, India

<sup>5</sup>Synchrotrons Utilization Section, Raja Ramanna Centre for Advanced Technology, Indore 452017, India

Received: 15 March 2022

Accepted: 15 July 2022

Published online:

13 August 2022

© The Author(s), under exclusive licence to Springer Science+Business Media, LLC, part of Springer Nature 2022

## ABSTRACT

We have investigated strain-induced spin lattice coupling in the CoFe<sub>2</sub>O<sub>4</sub>/0.65Pb (Mg<sub>1/3</sub>Nb<sub>2/3</sub>)O<sub>3</sub>–0.35PbTiO<sub>3</sub>(PMN-PT) composite system, evident by temperature-dependent Raman spectroscopy and magnetization measurements. The strain interactions lead to magneto-electric coupling, and the measured magneto-electric voltage coefficient is 40 mV/cm<sup>-1</sup>Oe<sup>-1</sup> for the CoFe<sub>2</sub>O<sub>4</sub>/PMN-PT composite samples. X-ray magnetic circular dichroism (XMCD) analysis establishes modified spin structure in the electrically poled CoFe<sub>2</sub>O<sub>4</sub>/PMN-PT composite, further validating the coupling between magnetic and electric ordering in the composite. The magneto-electric coupling coefficient  $\alpha$  vs dc magnetic field curves revealed hysteretic behavior and enhanced  $\alpha$  values after electric poling, which originates from the strain-induced modifications in the magnetic structure of composite in the electrically poled samples. These findings suggest that the existence of spin lattice coupling may lead to the mechanism of strong magneto-electric effects via strain interactions in CoFe<sub>2</sub>O<sub>4</sub>/PMN-PT composite.

## 1 Introduction

Recently, multiferroic composites exhibiting strong magneto-electric(ME) effects at room temperature have attracted tremendous attention for developing

fascinating device concepts for spintronics and memory storage applications. The ME composites permit modification in the electric polarization by a magnetic field (direct ME effect) or the magnetization by an applied electric field (converse ME effect) [1, 2].

Address correspondence to E-mail: anjahlawat@gmail.com

Ferroelectric materials with high piezoelectric coefficients and ferromagnetic materials with high magnetostriction are suitable candidates to achieve strong ME effects in multiferroic composites, such as  $\text{NiFe}_2\text{O}_4/\text{Pb}(\text{Mg}_{1/3}\text{Nb}_{2/3})\text{O}_3\text{-PbTiO}_3$  (NFO-PMNPT),  $\text{PbZrTiO}_3\text{-CoFe}_2\text{O}_4$  (PZT-CFO),  $\text{PbTiO}_3\text{-CoFe}_2\text{O}_4$  (PTO-CFO),  $\text{BaTiO}_3\text{-CoFe}_2\text{O}_4$  (BTO-CFO), etc. [3–5].

Owing to the correlated crystal and magnetic structures, the ME coupling in multiferroic composites, which is quantified as ME voltage coefficient ( $\alpha$ ), depends mainly on the strain transfer at the interface between the ferroelectric/piezoelectric and ferromagnetic/magnetostrictive phase [5–8]. Generally, X-ray diffraction (XRD) and Raman spectroscopy are used to probe the induced strain lattice distortion and correlations between lattice and spin dynamics [9, 10], as shown in our previous studies also on  $\text{NiFe}_2\text{O}_4/\text{PMN-PT}$  composites [11, 12], wherein we observed modification in the crystal structure across the ferroelectric transition temperature of PMN-PT (owing to the strain transfer from PMN-PT to  $\text{NiFe}_2\text{O}_4$ ). Further, the magnetic structure can also be modified due to the interfacial strain transfer from the ferroelectric phase to the magnetic phase [13]. Such strain-induced modifications in crystal and magnetic structure in multiferroic composites help to comprehend the mechanism of ME coupling.

In this work, we have investigated the spin–lattice correlations in strain-coupled magneto-electric multiferroic  $\text{CoFe}_2\text{O}_4/0.65\text{Pb}(\text{Mg}_{1/3}\text{Nb}_{2/3})\text{O}_3\text{-}0.35\text{PbTiO}_3$  (PMN-PT) composite. PMN-PT is a robust ferroelectric material and exhibits structural phase transition ( $P4mm$  to  $Fm\bar{3}m$  space group) at its Curie temperature ( $T_C$ )  $\sim 450$  K [14].  $\text{CoFe}_2\text{O}_4$  (CFO) is a known ferrimagnetic material with high magnetostriction ( $\lambda = 200\text{--}400$  ppm) and becomes paramagnetic beyond  $\sim 870$  K [15]. The chosen materials have good interface linking and hence display an effective strain transfer to the CFO phase upon the structural transition of PMN-PT.

Many synthesis methods have been used to fabricate spinel ferrite  $\text{CoFe}_2\text{O}_4$  such as the mechano-synthesis, the hydrothermal method, synthesis by solution combustion, synthesis by co-precipitation, the solid-state reaction, sol–gel synthesis, and the sol–gel auto-combustion method. Among these methods, Sol–gel technique is found to be more appropriate than the others. The sol–gel combustion method employs a self-sustaining exothermic reaction

between an oxidant agent and fuel which allows achieving high temperatures in short reaction times. The experimental conditions used in these methods of preparation play an important role on the properties and the particle size of the ferrite nanoparticles.

In our previous study on NFO/PMN-PT, we studied strain-induced magneto-electric effect, here we would like to emphasize that although the  $\text{NiFe}_2\text{O}_4$  and  $\text{CoFe}_2\text{O}_4$  exhibit nearly similar crystal structure (inverse spinel), the magnetic properties are quite different;  $\text{NiFe}_2\text{O}_4$  is a soft ferrimagnet, whereas  $\text{CoFe}_2\text{O}_4$  is hard ferrimagnet material and its magnetostriction is higher as compared to  $\text{NiFe}_2\text{O}_4$  [16, 17]. It should be noted that magnetostriction is an important factor in determining the magneto-electric properties of strain-coupled multiferroic composites. The higher magnetostriction in the  $\text{CoFe}_2\text{O}_4/\text{PMN-PT}$  system is expected to significantly enhance the magneto-electric properties.

Therefore, it is appealing to study magneto-electric properties of the  $\text{CoFe}_2\text{O}_4/\text{PMN-PT}$  system and probe its origin. In this context, we studied strain-induced changes in crystal and magnetic structure of the  $\text{CoFe}_2\text{O}_4$  and the correlations between lattice and spin dynamics, which is considered as a figure of merit in the magneto-electric coupled systems. The spin–phonon coupling in the strain-coupled  $\text{CoFe}_2\text{O}_4/\text{PMN-PT}$  composite samples has not been studied so far.

## 2 Experimental

### 2.1 Synthesis

The nanocomposite of the molar ratio of 0.70 (PMN-PT)–0.30 (CFO) was prepared by mixing parent nanopowders of CFO and PMN-PT. All precursor chemicals were of analytical grade and used as received without further purifications. CFO nanopowder was prepared using a citric acid-based sol–gel combustion method [18]. Iron nitrate ( $\text{Fe}(\text{NO}_3)_3 \cdot 9\text{H}_2\text{O}$ , 98.5%), cobalt nitrate ( $\text{Co}(\text{NO}_3)_2 \cdot 6\text{H}_2\text{O}$ , 99%), and citric acid ( $\text{C}_6\text{H}_8\text{O}_7$ , 99.5%), all from Aldrich, were used as the starting materials and deionized water was used as solvent. Stoichiometric amounts of cobalt and Iron nitrate were dissolved in deionized water separately. Citric acid and the cobalt nitrate solution were successively mixed to Iron nitrate solution (The molar ratio of metal cation

(Fe + Co) and citric acid was kept at 1:1.2). The sol was obtained by stirring the mixed nitrate solution until it became a transparent liquid. Ammonia solution was then added dropwise to make the pH value of mixture to be nearly 8. The dry gel was obtained by stirring the sol at 70 °C for about 2 h and dried for 20 h at 120 °C. The precursor powders were obtained by the auto-combustion method.

PMN-PT nanopowder was prepared using a wet chemical method, as explained in detail elsewhere [19]. The individually prepared powders of CFO and PMN-PT were mixed and grounded for 5 h. The fine grounded powder of the mixture was pelletized and sintered at 750 °C for 10 h.

## 2.2 Used experimental technique

The crystal structures of the samples were analyzed by the X-ray diffraction (XRD) technique using synchrotron source ( $E = 15.431$  keV). Scanning electron microscopy (SEM) measurements were carried out for microstructure analysis. Raman spectroscopy measurements were carried out using Horiba JobinVyon, micro-Raman spectrometer (488 nm excitation laser), equipped with an edge filter for Rayleigh line rejection, and a CCD detector. The spectral resolution was  $\sim 1$  cm<sup>-1</sup>. The magnetic measurements were performed using Quantum Design SQUID-VSM. The dielectric measurements were performed using a Novocontrol impedance analyzer. X-ray absorption spectra (XAS) and X-ray magnetic circular dichroism (XMCD) were measured at the Fe and Ni  $L_{2,3}$  edges at room temperature in total electron yield mode at polarized light soft x-ray absorption beamline BL1 at Indus-2 synchrotron source, RRCAT, Indore (INDIA). XMCD spectra were obtained at an applied field of  $\pm 1$  T and fixed helicity of the incident photon beam. The magneto-electric coupling coefficient measurements were performed by changing the bias magnetic field (1 T) under application of  $H_{ac} = 10$  Oe (at frequency = 10 kHz) produced using Helmholtz coils. The voltage output generated from the composite was measured by the lock-in amplifier (Stanford, SR532); the reference signal was taken from the signal generator feeding the Helmholtz coils.

## 3 Results and discussion

### 3.1 Crystallographic phase analysis

Figure 1a shows Rietveld refined XRD pattern of PMN-PT/CFO composite measured at 300 K. The refinement analysis reveals tetragonal structure (space group—P4mm) of PMN-PT and cubic inverse spinel (space group—Fd-3 m) of CFO in the composite. Room-temperature crystal symmetry of the two phases in the composite is further confirmed by Raman spectroscopy, as shown in Fig. 1b. The phonon modes  $E_g + 3T_{2g} + A_{1g}$  correspond to CFO inverse spinel structure with space group  $O^7h$  ( $Fd\bar{3}m$ ) [20]. The peaks observed for PMN-PT are mainly attributed to longitudinal optical (LO) modes, i.e.,  $A_1$  and E modes of tetragonal PMN-PT (Fig. 1b) [21]. The Raman modes of the composite are slightly shifted in the position as compared to the individual PMN-PT and CFO. The  $E(LO_2)$  modes of PMN-PT phase show a redshift, while  $A_{1g}$  phonon mode of the CFO phase exhibits a blue shift. It indicates that CFO undergoes compression, while PMN-PT lattice experiences tensile strain in the composite, concomitant with the XRD results where CFO peaks are shifted toward lower  $2\theta$  side and PMNPT reflections are shifted toward higher  $2\theta$  values, as shown in inset of Fig. 1b. It divulges that PMN-PT and CFO are coupled via elastic interactions in the composite via strain transfer through the interfaces between piezoelectric PMN-PT and magnetostrictive CFO. Figure 1c represents SEM image indicating large grains of  $\sim 1$ –2 micron corresponding to the PMN-PT phase and small nanoparticles of CFO ( $\sim 100$ –200 nm) corresponding to the PMNPT phase. The individual phases were confirmed by energy-dispersive X-ray (EDAX) analysis.

### 3.2 Temperature-dependent XRD and Raman spectroscopy analysis

Across  $T_C$ , the structural phase transition of PMN-PT will influence the adjacent lattice of CFO, which can be realized from the temperature-dependent XRD measurements. Figure 2a shows that XRD patterns of the CFO/PMN-PT nanocomposite were measured at different temperatures 300 K, 400 K, and 500 K (i.e., across  $T_C$  of PMN-PT). Figure 2b, c shows an enlarged view in the selected  $2\theta$  range of  $16^\circ$ – $19.5^\circ$  and  $21.8^\circ$ – $23.8^\circ$ . Figure 2c indicates diffraction peaks

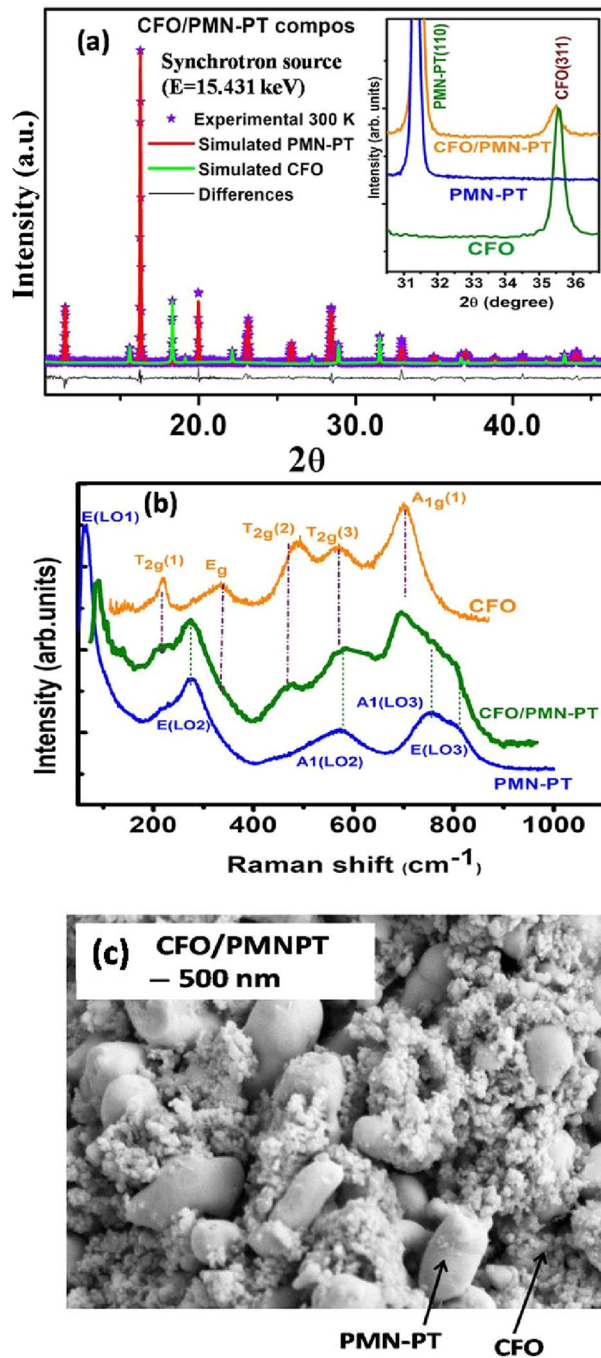


**Fig. 1** **a** Room-temperature rietveld refined XRD pattern of CFO/PMN-PT composite at, **b** room-temperature Raman spectra of pure CFO, pure PMN-PT, and composite CFO/PMN-PT, inset shows enlarged view of XRD pattern of pure CFO, pure PMN-PT, and CFO/PMN-PT composites in a selected  $2\theta$  range of 30.7–36.7 degree, **c** SEM image of the CFO/PMN-PT composite

corresponding to CFO (400) reflection and PMN-PT (200) reflection. Owing to the structural transition of PMN-PT at 450 K, it is observed that the doublet in

(200) reflection of PMN-PT at 300 K corresponding to the tetragonal phase changes to a single Bragg peak P(200) at 500 K corresponding to cubic  $Pm\bar{3}m$  phase, [22, 23]. From the XRD analysis of CFO phase in composite (Fig. 2b), it is observed that the intensity ratio  $I_{(220)}/I_{(222)} = 4.25$  at 400 K changes considerably to 5.16 at 500 K. It should be noted that in inverse spinel ferrites, e.g.,  $NiFe_2O_4$ ,  $CoFe_2O_4$ ,  $I_{(220)}/I_{(222)}$  ratio depends on the cations occupying the A sites and B sites [24–27]. This observation reveals the modification in Co/Fe distribution at the T and O sites in CFO phase of the composite across  $T_C$  of PMN-PT, which is further confirmed from the temperature-dependent Raman spectra studies (Fig. 3a). It is well known that  $A_{1g}$  modes and  $T_{2g}$  (2) mode are highly sensitive to the cations ( $Co^{2+}/Fe^{3+}$  ions) distribution at T and O sites, respectively [24–27]. The mode position and line width of  $A_{1g}$  and  $T_{2g}$  (2)

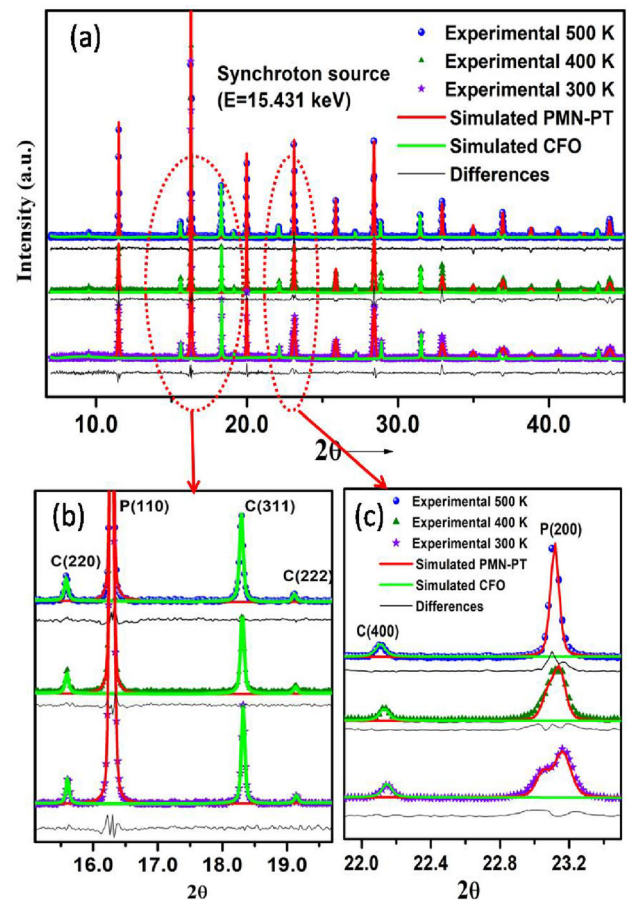


**Fig. 2** Rietveld refined comparative XRD pattern of CFO/PMN-PT composite collected at different temperatures, i.e., 300 K, 400 K, and 500 K; **b** enlarged view in the selected  $2\theta$  range of 15.7°–19.7°; **c** enlarged view in the selected  $2\theta$  range of 21°–25°

modes demonstrate deviation from usual anharmonic behavior [28] and exhibit strong anomalies around  $T_C \sim 450$  K of PMN-PT (Fig. 3b–e). These observations divulge lattice instabilities in CFO across  $T_C$ , which arise due to strain transfer through interface induced by the structural transformation in PMN-PT.

Any kind of change in the cation inversion in CFO affects the relative intensity of ( $A_{1g}(1) + A_{1g}(2)$ ) modes in (doublet at  $\sim 700$   $\text{cm}^{-1}$ ) [24–26]. The relative intensity of  $A_{1g}(1)$  and  $A_{1g}(2)$  modes represents cation inversion, which can be written as  $X_{\text{Fe}/\text{Co}}$ , where  $X$  represents cation inversion factor. The parameter  $X_{\text{T/O}}$  equals to 0 when there is no cation inversion and equals to 1 if the cation inversion is complete. Figure 4a shows a plot of the relative intensity, i.e.,  $\frac{I_{A_{1g}(1)}}{I_{A_{1g}(1)+A_{1g}(2)}}$  ( $= X_{\text{T/O}}$ ) as a function of temperature, which reveals  $X_{\text{T/O}}$  to be nearly constant upto  $T_C \sim 450$  K and it drops suddenly beyond  $T_C$ . This divulges that Co/Fe distribution in CFO phase of the composite is modified beyond 450 K, concomitant with the XRD studies (Fig. 2b). Figure 4b, c presents spectral deconvolution of the composite across the selected temperature region (300 K and 500 K) where the strongest anomalies are observed in Raman peak positions and line width. These modifications in CFO phase arise owing to the structural transition of PMN-PT at  $\sim 450$  K, which causes a strain on the adjacent lattice of CFO in the composite and modifies its lattice. Earlier such kind of modification in cation distribution at the T and O sites was reported in pressure-dependent studies on CFO [20, 26, 27].

**Fig. 3** a Temperature-dependent Raman spectra of CFO/PMN-PT composite; temperature dependence of the phonon mode (b, c) positions and d, e width of T-site ( $A_{1g}$ ) and O-site ( $T_{2g}(2)$ ) modes observed for composite CFO/PMN-PT

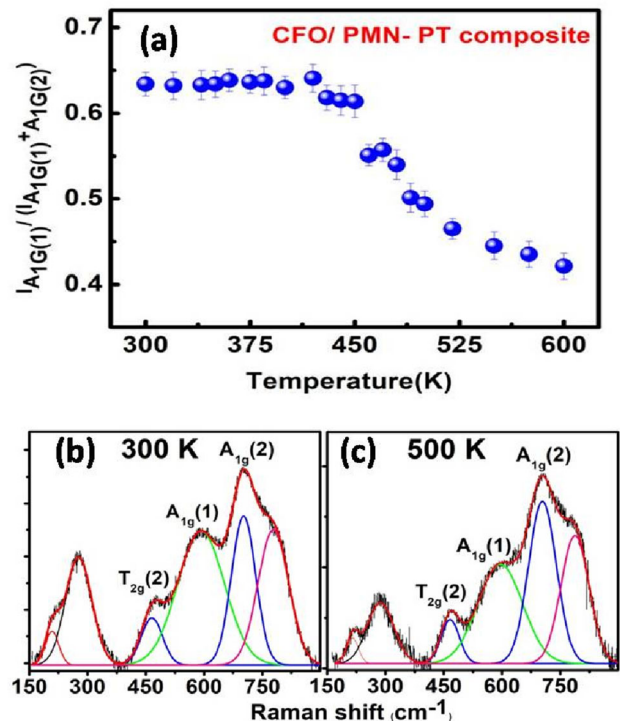
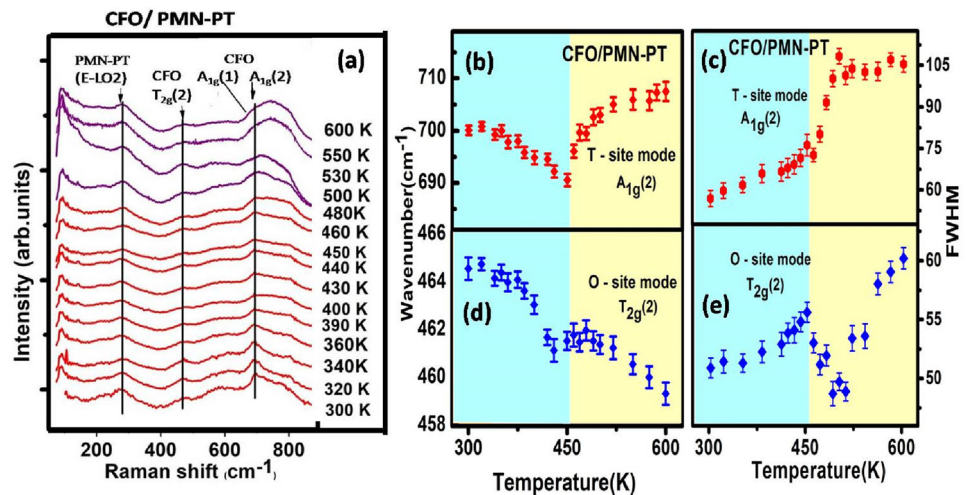


**Fig. 4** Temperature evolution of the intensity ratio  $\frac{I_{A_{1g}(1)}}{I_{A_{1g}(1)+A_{1g}(2)}}$  of  $A_{1g}(1)$  and  $A_{1g}(2)$  phonon modes for CFO/PMN-PT composite in the temperature range 300 K–600 K; b–c temperature-dependent spectral deconvolution for selected frequency range of CFO/PMN-PT composite at 300 K and 500 K. The points show experimental data and the solid line represents the results of fitting of the phonon modes by multiple Lorentzian line shape function

### 3.3 Correlation between magnetization and phonon behavior

The temperature-dependent magnetization was measured in field-cooled warming (FCW) mode

under the applied magnetic field of 100 Oe, for CFO and CFO/PMN-PT composite, as shown in Fig. 5a. CFO exhibits a characteristic ferrimagnetic behavior with gradual increase in magnetization as the temperature is lowered below its magnetic ordering temperature 750 K [22]. However, the CFO/PMN-PT composite shows an unusual drop in the magnetic moment around  $T_C$ -450 K of PMN-PT. The  $T_C$  of PMN-PT is indicated by a peak in the temperature-dependent dielectric constant around 450 K (Fig. 5b). The abrupt change in magnetization can be attributed to the lattice instabilities in CFO near  $T_C$  of PMN-PT, which are quite evident from the phonon behavior (frequencies and line width of  $A_{1g}$  and  $T_{2g}(2)$  phonon modes) near 450 K.

The correlation of anomalous phonon behavior with magnetization can be better exemplified via spin-phonon coupling, caused by the phonon modulation of spin exchange integral [28, 29]. Granado's et al. proposed that the phonon renormalization at magnetic ordering temperature is proportional to the nearest neighbor spin-spin correlation function and scales with the square of the sublattice magnetization [28]. Accordingly, the spin-phonon coupling can be evaluated by the spin correlation functions  $\langle S_i \cdot S_j \rangle$  (where  $S_i$  and  $S_j$  are the localized spins at the  $i$ th and  $j$ th sites), which leads to

$$\Delta\omega(T) = \omega_{anh}(T) - \omega(T) \propto (M^2(T)/M_{max}^2), \quad (1)$$

where  $M(T)$  is the average magnetization per magnetic ion,  $M_{max}$  is the saturation magnetization. Figure 5c clearly shows that the temperature-dependent phonon frequency shift ( $\Delta\omega(T)$ ) of  $T_{2g}(2)$  mode of CFO phase in the composite scales with the square of its magnetization  $(M^2(T)/M_{max}^2)$ , demonstrating the spin-phonon coupling in the composite unambiguously. The spin-phonon coupling imprints its effect on the magneto-electric character also. The ME effect is evident from Fig. 5a, b, where the concurrence between dielectric and magnetic ordering behavior can be observed, indicating toward a possible ME coupling.

### 3.4 Evidence of magneto-electric coupling analysis

In order to confirm the existence of ME coupling in CFO/PMN-PT composite, the magnetization as a function of magnetic field ( $M - H$ ) was measured

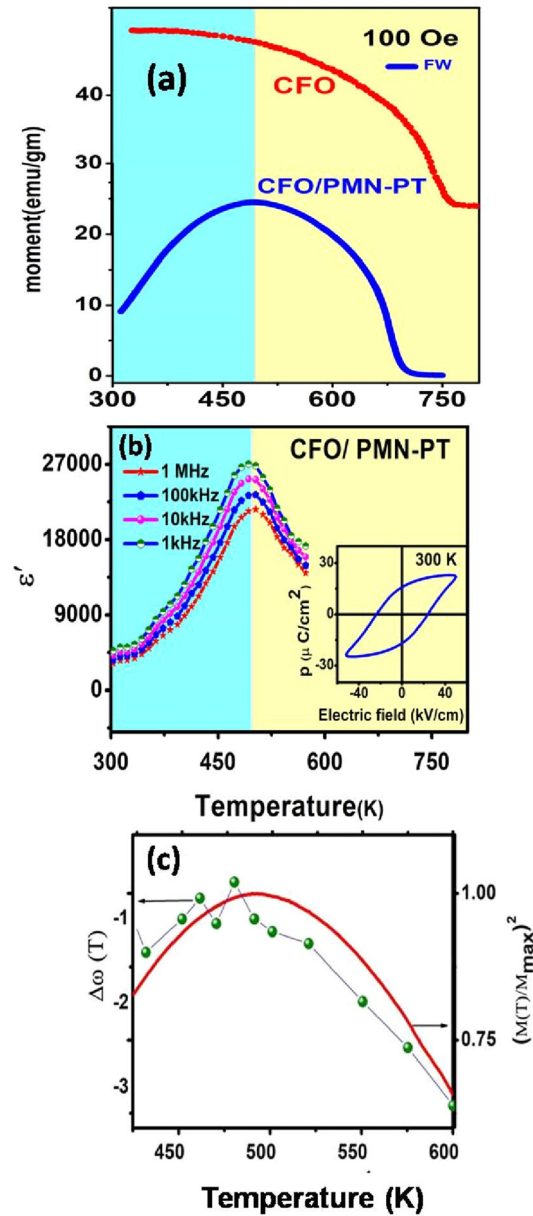


**Fig. 5** Temperature-dependent magnetization curve measured at  $H = 100$  Oe for pure CFO and CFO/PMN-PT composite; **b** temperature-dependent dielectric constant measured at various frequencies for composite, inset shows the polarization vs electric field, inset shows (PE) loop for CFO/PMN-PT composite **(c)** comparison of  $(M(T)/M_{max})^2$  and  $(\Delta\omega(T))$  as a function of temperature

before and after electrical poling at an applied electric field of  $E = + 40$  kV/cm, as shown in Fig. 6a. The applied electric field was above the coercive field ( $E_C \sim 23$  kV/cm) of CFO/PMN-PT composite at room temperature (inset Fig. 5b). The conductivity and loss tangent are of the order  $10^{-9} \Omega^{-1} \text{ cm}^{-1}$  and

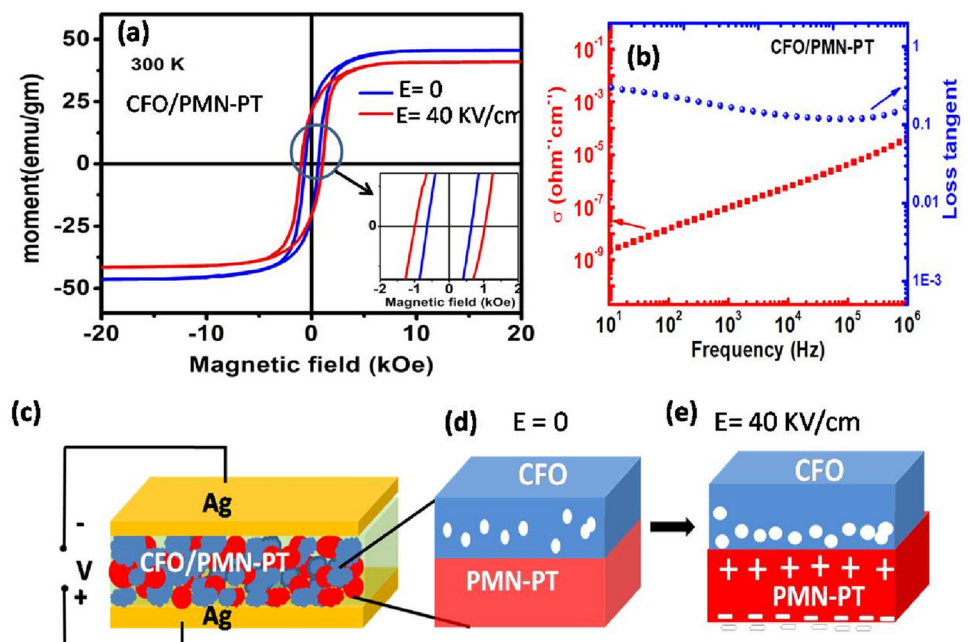
0.21 at frequency 1 kHz, respectively (Fig. 6b). It is observed that after electric poling, saturation magnetization decreases from 44 to 39.5 ( $\pm 0.2$ ) emu/g and coercivity of the composite increases drastically. Poled composite sample exhibits non-volatile changes in the magnetization, i.e., it does not revert back to its initial value after the removal of electric field.

The electric field leads to the ferroelectric dipoles alignment along the electric field direction, and consequently, the ferroelectric/piezoelectric PMN-PT experiences elongation in the field direction which produces stress in the magnetostrictive CFO phase in the composite sample. The induced stress modifies the crystalline arrangement as well as spin and orbital degrees of freedom [30, 31]. Hence, the electric field-induced strain can alter the magnetization of the composite. Also, the electric field causes accumulation of electrons/holes at the interface of PMN-PT and CFO, which would attract/repel the oxygen vacancies at the CFO/PMN-PT interfaces. This leads to redistribution of oxygen vacancy in the poled samples, as described in the schematic of Fig. 6c. The magnetic structure of CFO consists of two anti-ferromagnetically ordered sublattices, i.e., A and B, corresponding to the tetrahedral ( $T_d$ ) and octahedral ( $O_h$ ) sites, respectively, with the  $Co^{2+}$  cations occupying  $O_h$  sites and the  $Fe^{3+}$  cations occupying equally both the  $T_d$  and  $O_h$  sites [32, 33]. The redistributions of oxygen vacancy can modify the  $M_s$  and  $H_c$  values

via changes in the superexchange interactions of A-O-B, A-O-A, and B-O-B and redistribution of local valences of cations ( $Fe^{2+}/^{3+}$ ,  $Co^{2+}/^{3+}$ ) at O and T sites in the CFO [31–33]. Thus, the altered magnetization in the poled CFO/PMN-PT may arise due to the collective effect of electric field-induced strain of PMN-PT, and charge modulation at the CFO/PMN-PT interfaces upon electric poling.

In this context, XMCD technique is used to study the spin structure (cationic sites distribution vis a vis magnetic moment at O and T sites) in poled and unpoled composite CFO/PMN-PT samples. XMCD provides detailed fingerprint of spinel structure where each specific cation (Fe/Co) generates a unique XMCD signature that is determined by its valence state (number of d electrons), site symmetry (i.e.,  $T_d$  or  $O_h$ ), and magnetization (local moment) direction [34]. Figure 7a–d presents XAS spectra of Fe and Co  $L_{2,3}$  edges with the helicity of incident X-ray parallel ( $\sigma^+$ ) and antiparallel ( $\sigma^-$ ) to the direction of magnetization and the corresponding XMCD signals for unpoled and poled composite samples, respectively. The  $L_3$  edge Fe XMCD signal (Fig. 7a) displays mainly three peaks where the first very small negative peak (A1) indicates contribution of  $Fe^{+2}$  at  $O_h$  site, next peak (A2) arises from  $Fe^{+3}$  at  $T_d$  site, and third negative peak (A3) is attributed to the  $Fe^{+3}$  ions at  $O_h$  site [35]. The opposite sign of A1 and A3 with respect to A2 implies that the magnetic moments of the  $Fe^{3+}$  ions in  $T_d$  symmetry are

**Fig. 6** **a** Room-temperature magnetization vs magnetic field ( $M - H$ ) loops measured for CFO/PMN-PT composite before and after electrical poling; **b** frequency-dependent conductivity and loss tangent curves for the unpoled CFO/PMN-PT composite; **c** schematic diagram for electric poling of CFO/PMN-PT composite; **d** unpoled state i.e., electric field ( $E = 0$ ); **e** poled state under application of  $E = 40$  kV/cm



coupled anti-ferromagnetically with the  $\text{Fe}^{3+}$  ions in  $\text{O}_h$  symmetry sites. A C2 feature with negative XMCD signal of  $L_3$  edge of Co edge (Fig. 7b) suggests that  $\text{Co}^{2+}$  ions occupy  $\text{O}_h$  sites. Appearance of feature C1 suggests that a small fraction of Co ions are residing at the  $\text{T}_d$  site also. The observed characteristic features of XMCD signal for the unpoled composite match well with CFO [35].

A linear combination of the simulated XMCD spectra using charge transfer multiplet calculations (CTM4XAS code [36]) is used to quantify the  $\text{Fe}^{2+}/^{3+}$  cations distribution at tetrahedral ( $\text{T}_d$ ) and octahedral ( $\text{O}_h$ ) sites. The analysis reveals 62%  $\text{Fe}^{3+}$  ions at  $\text{O}_h$  sites, 30%  $\text{Fe}^{3+}$  ions at  $\text{T}_d$  sites, and a small fraction (8%) of  $\text{Fe}^{2+}$  ions occupy  $\text{O}_h$  sites, for the unpoled CFO/PMNPT composite. While for the poled composite samples, 55%  $\text{Fe}^{3+}$  ions are at  $\text{O}_h$  sites, 40%  $\text{Fe}^{3+}$  ions at  $\text{T}_d$  sites, and a small fraction (5%) of  $\text{Fe}^{2+}$  ions occupy  $\text{O}_h$  sites. It suggests that a fraction of  $\text{Fe}^{3+}$  ions are

transferred from  $\text{O}_h$  to  $\text{T}_d$  site after electric field poling. The comparison of the Co  $L_{2,3}$  edges XMCD signal for poled and unpoled PMN-PT/CFO reveals that the C2 peak intensity is reduced and a small positive peak (C1) at 778 eV in unpoled sample is missing in the poled sample. These observations suggest that while CFO in unpoled sample possesses mixed inverse spinel structure, it gradually moves toward inverse spinel structure upon electric poling, which also modifies the magnetic properties of CFO in poled CFO/PMN-PT samples. This further suggests that the electric field poling leads to the redistribution or introduction of oxygen vacancies in the CFO through CFO/PMN-PT interfaces. Figure 8 shows schematic representation of cations ( $\text{Fe}^{3+}/\text{Co}^{2+}$ ) redistribution in normal spinel and mix spinel structure of CFO.

Further, the orbital ( $m_l$ ) and spin ( $m_s$ ) contributions to the total magnetic moment per cation for the poled and unpoled composite samples can be estimated by

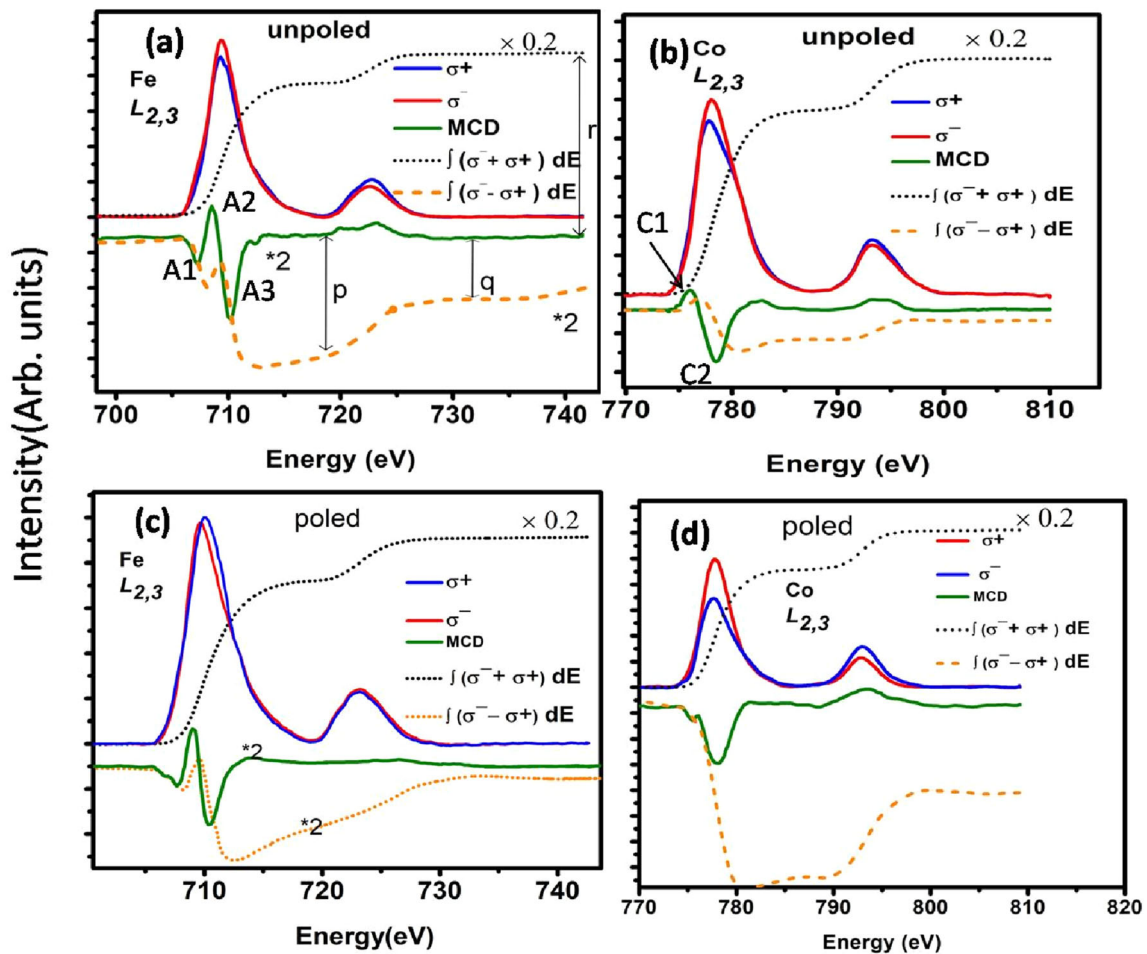


**Fig. 7** XMCD signal measured at the Fe (a) and Co (b)  $L_{2,3}$  edges, for unpoled composite samples; c XMCD signal for Fe and d  $\text{Co}L_{2,3}$  edges, for electrically poled composite sample



sum rule [37, 38], which allow the evaluation of average total magnetic moment ( $m = m_l + m_s$ ) of the Co and Fe ions.

$$m_l = -\frac{4}{3}N^h \frac{q}{r} \quad (2)$$

$$m_s + \langle T_z \rangle \geq -N^h \left( \frac{6p - 4q}{r} \right), \quad (3)$$

where  $m_l = -\frac{4}{3}N^h \frac{q}{r}$

$$r = \int_{L_{2,3}} (\sigma^+ + \sigma^-) dE, p = \int_{L_3} (\sigma^+ - \sigma^-) dE, q = \int_{L_{2,3}} (\sigma^+ - \sigma^-) dE$$

$N^h$  represents the number of 3d band holes,  $p$  is the integral of the XMCD signal for the L3 edge,  $q$  is the integral of the XMCD signal for the L3 and L2 edges, and  $r$  is the integral of the average XAS spectrum. The Eq. (2) is directly used to calculate the  $m_l$ , while an effective  $m_s$  is estimated (using Eq. (3)) by including the expectation value of the magnetic dipole operator ( $\langle T_z \rangle$ ), which is negligible for transition metal compounds at room temperature and hence neglected in the present case [39].

In unpoled sample, the value of Co  $m_s$  is estimated to be  $0.32 \mu_B$  and  $m_l = 0.03 \mu_B$ , yielding the magnetic moment contribution due to Co ion  $M_{Co} = 0.35 \mu_B$ . Similarly for the Fe ions,  $m_s = 3.1 \mu_B$  and  $m_l = 0.19 \mu_B$ , and total  $M_{Fe} = 3.29 \mu_B$ . Hence, the net magnetic moment for the unpoled sample is estimated to be  $\sim 3.64 \mu_B$ . The total moment is slightly higher than expected values for CFO ( $3 \mu_B$ ) having inverse spinel structure, which is consistent with the somewhat mixed spinel structure of CFO as evident from the XAS data analysis. For the poled samples, we estimate  $M_{Co} = 2.46 \mu_B$  ( $m_s = 2.10 \mu_B$ ,  $m_l = 0.36 \mu_B$ ), and  $M_{Fe} = 0.73 \mu_B$  ( $m_s = 0.70 \mu_B$ ,  $m_l = 0.03 \mu_B$ ), yielding total moment  $3.19 \mu_B$ . This is consistent with our XAS observation that upon electric poling, the system has a tendency to adopt an inverse spinel structure, wherein the magnetic moment of CFO is largely attributed to the Co ions as Fe ions moments cancel each other. It is noted that after poling the relative contribution of spin and orbital magnetic moment changes considerably. These results establish coupling between electric and magnetic ordering in the CFO/PMN-PT composite samples, as the application of electric field causes redistribution of cations at  $O_h$  and  $T_d$  sites.

Moreover, the coupling can be quantified in terms of the magneto-electric coefficient ( $\alpha$ ) measured as a

function of in-plane  $H_{dc}$  at an off-resonance frequency of 10 kHz under superimposed in-plane ac magnetic field ( $H_{ac}$ ) of 10 Oe, as shown in Fig. 9a, b. Interestingly, the unpoled composite also reveals ME coefficient (Fig. 9a) as the two phases are strain coupled with each other. The poled composites show enhanced  $\alpha$  value, clear hysteresis behavior with coercive field of  $\sim 4000$  Oe as well as remnant  $\alpha$  value of  $40 \text{ mV/cm}^{-1} \text{Oe}^{-1}$  (Fig. 9b), establishing self-biased ME effect [40] in CFO/PMN-PT nanocomposite. The self-biased hysteretic behavior can be explained from effective magnetostriction ( $\lambda$ ) behavior [41] (Fig. 9c, d), which is estimated by integrating  $\alpha$  with respect to the  $H_{dc}$  [as  $\alpha$  is proportional to piezomagnetic coefficient ( $q = d\lambda/dH_{dc}$ )]. For the unpoled sample,  $\lambda$  remains unchanged at  $H_{dc} = 0$  under small variation of magnetic field ( $\delta H_{ac}$ ) (Fig. 9c) suggesting that magnetic domain cannot move easily in this condition and restrict domain wall migration. Whereas poled composite exhibits asymmetric  $\lambda$  curves where  $\lambda$  has a finite value (with  $\delta H_{ac}$ ) at  $H_{dc} = 0$  (shown by dotted lines in Fig. 9d), implying easy domain rotation under  $\delta H_{ac}$  or  $\delta \Gamma_{ac}$  ( $\Gamma_{ac} = \text{stress}$ ) and hence effective strain generation/transfer. Indeed, the interactions between built-in bias ( $H_{int}$ ) and  $H_{dc}$  cause shift and asymmetrical behavior of effective  $\lambda$ , resulting in self-biased ME effects [42]. The effective dc magnetic bias ( $H_{Eff} = H_{int} + H_{dc}$ ) in CFO/PMN-PT composite strongly depends upon the relative orientation of  $H_{int}$  and  $H_{dc}$ . This causes different maximum  $\alpha$  value at different  $H_{Eff}$  during the reverse and forward sweep [41, 42].

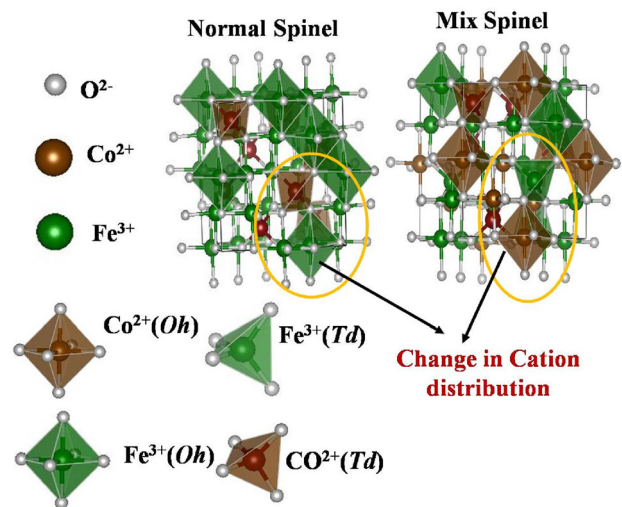


**Fig. 8** Schematic representation of cations ( $\text{Fe}^{3+}/\text{Co}^{2+}$ ) redistribution in normal spinel and mix spinel structure of CFO

Hence, the ME hysteretic behavior w.r.t external  $H_{dc}$  is governed by the piezomagnetic coefficient's dependence on the  $H_{Eff}$ .

From these observations, it can be concluded that whether the strain is induced via ferroelectric transitions or applied electric field, it is effectively transferred to the adjacent magnetic phase through interfaces and modifies its crystal and magnetic structure, resulting in the strong coupling between electric and magnetic order parameters in such composites.

### 4 Conclusion

In conclusion, we have investigated the strain-induced magneto-electric effects and the modification in the structure of individual  $CoFe_2O_4$  and PMN-PT due to strain transfer across the interfaces. It is revealed that the interfacial strain in CFO phase developed across the ferroelectric/structural transition ( $T_C \sim 450$  K) of PMN-PT causes local lattice instabilities in CFO lattice and induces spin-phonon coupling. The room-temperature magneto-electric coupling was evidenced by measuring M-H loops for the unpoled and electrically poled CFO/PMN-PT composite. XMCD studies reveal modified spin structure in the electric poled composite at room temperature. Interestingly, electrically poled composites reveal improved ME coefficient  $\alpha$  values with

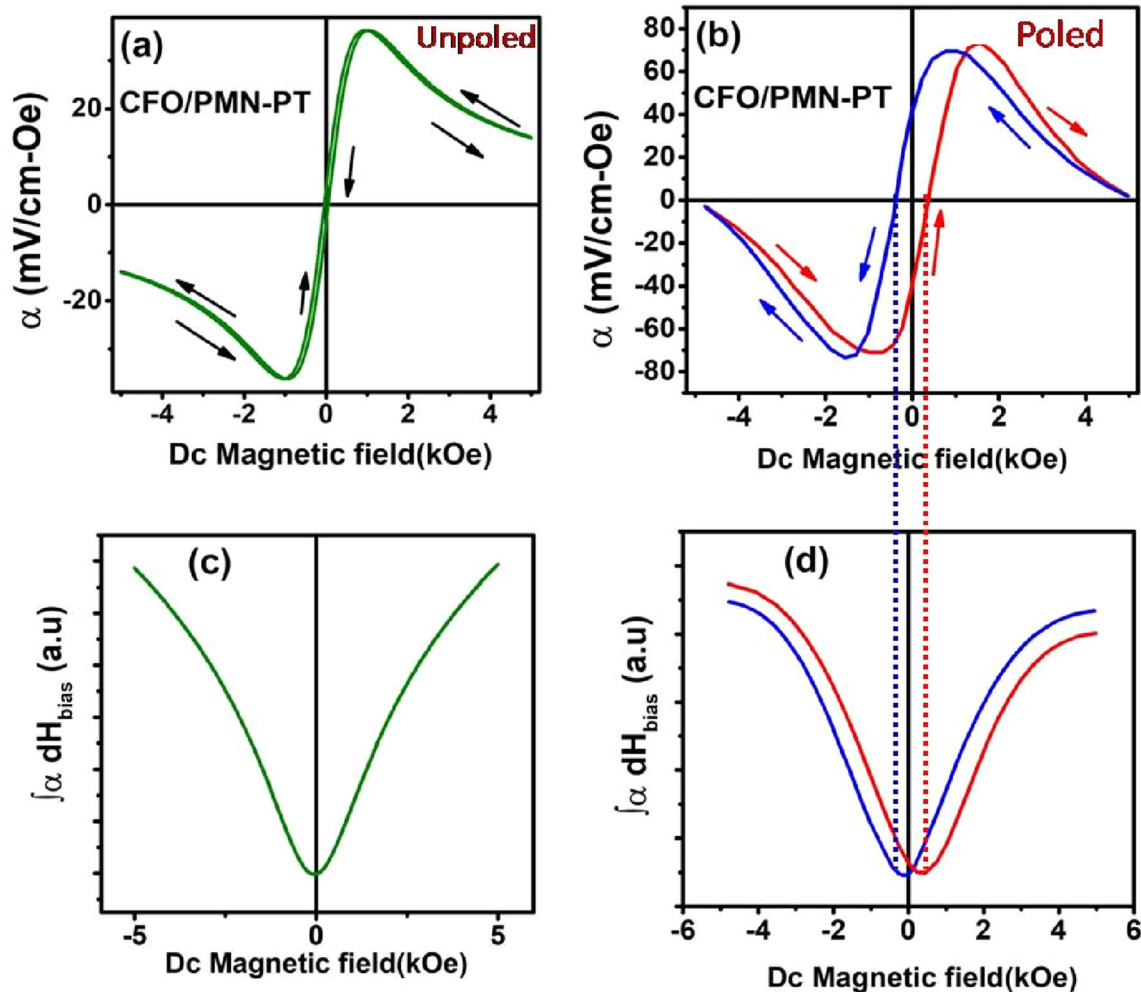


**Fig. 9** Magnetic DC field-dependent magneto-electric coefficient ( $\alpha$ ) for **a** unpoled CFO/PMN-PT, **b** poled CFO/PMN-PT, **c** integral values of  $\alpha$  with respect to the  $H_{bias}$  for unpoled CFO/PMN-PT, **d** poled CFO/PMN-PT

self-biasing ME effects as compared to unpoled composites, owing to the modification in the magnetic domain structure of composite after electric poling.

## 5 Data availability statement

The data that support the findings of this study are available within the article.

## Acknowledgements

The authors would like to acknowledge (CSIR), New Delhi, India for financial support. The authors thank Mr. Manvendra Narayan Singh for assistance in high-temperature XRD measurement, Mr. Rakesh Shah and Mr. Avnish Wadikar for XMCD measurement at Indus beamline, RRCAT, Indore.

## Author contributions

All authors contributed to the study conception and design. Material preparation, data collection, and analysis were performed by AA and AAK. The first draft of the manuscript was written by AA and all authors commented on the manuscript. All authors read and approved the final manuscript.

## Funding

Central Mechanical Engineering Research Institute, Council of Scientific and Industrial Research, grant no. B-12735.

## Declarations

**Conflict of interest** The authors have no conflicts to disclose.

## References

- C.W. Nan, M.I. Bichurin, S. Dong, D. Viehland, G. Srinivasan, Multiferroic magnetoelectric composites: historical perspective, status, and future directions. *J. Appl. Phys.* **103**, 31101 (2008). <https://doi.org/10.1063/1.2836410>
- W. Eerenstein, M. Wiora, J.L. Prieto, J.F. Scott, N.D. Mathur, Giant sharp and persistent converse magnetoelectric effects in multiferroic epitaxial heterostructures. *Nat. Mater.* **6**, 348–351 (2007). <https://doi.org/10.1038/nmat1886>
- Z. Li, Y. Wang, Y. Lin, C. Nan, Evidence for stress-mediated magnetoelectric coupling in multiferroic bilayer films from magnetic-field-dependent Raman scattering. *Phys. Rev. B* **79**, 180406 (2009). <https://doi.org/10.1103/PhysRevB.79.180406>
- I. Levin, J. Li, J. Slutsker, A.L. Roytburd, Design of self-assembled multiferroic nanostructures in epitaxial films. *Adv. Mater.* **18**, 2044–2047 (2006). <https://doi.org/10.1002/adma.200600288>
- W.S. Ferreira, J. Agostinho Moreira, A. Almeida, M.R. Chaves, J.P. Araújo, J.B. Oliveira, J.M. Machado Da Silva, M.A. Sá, T.M. Mendonça, P. Simeão Carvalho, J. Kreisel, J.L. Ribeiro, L.G. Vieira, P.B. Tavares, S. Mendonça, Spin-phonon coupling and magnetoelectric properties:  $\text{EuMnO}_3$  versus  $\text{GdMnO}_3$ . *Phys. Rev. B* **79**, 54303 (2009). <https://doi.org/10.1103/PhysRevB.79.054303>
- J. Laverdière, S. Jandl, A.A. Mukhin, V.Y. Ivanov, V.G. Ivanov, M.N. Iliev, Spin-phonon coupling in orthorhombic  $\text{RMnO}_3$  ( $R=\text{Pr, Nd, Sm, Eu, Gd, Tb, Dy, Ho, Y}$ ): a Raman study. *Phys. Rev. B* **73**, 214301 (2006). <https://doi.org/10.1103/PhysRevB.73.214301>
- T. Goto, T. Kimura, G. Lawes, A.P. Ramirez, Y. Tokura, Ferroelectricity and giant magnetocapacitance in perovskite rare-earth manganites. *Phys. Rev. Lett.* **92**, 257201 (2004). <https://doi.org/10.1103/PhysRevLett.92.257201>
- T. Kimura, S. Ishihara, H. Shintani, T. Arima, K.T. Takahashi, K. Ishizaka, Y. Tokura, Distorted perovskite with  $e_g 1$  configuration as a frustrated spin system. *Phys. Rev. B* **68**, 60403 (2003). <https://doi.org/10.1103/PhysRevB.68.060403>
- K.D. Truong, J. Laverdière, M.P. Singh, S. Jandl, P. Fournier, Impact of Co/Mn cation ordering on phonon anomalies in  $\text{La}_2\text{CoMnO}_6$  double perovskites: Raman spectroscopy. *Phys. Rev. B* **76**, 132413 (2007). <https://doi.org/10.1103/PhysRevB.76.132413>
- A. Ahlawat, S. Satapathy, V.G. Sathe, R.J. Choudhary, P.K. Gupta, Evidence of spin phonon coupling in magnetoelectric  $\text{NiFe}_2\text{O}_4/\text{PMN-PT}$  composite. *Appl. Phys. Lett.* **103**, 252902 (2013). <https://doi.org/10.1063/1.4850555>
- A. Ahlawat, S. Satapathy, V.G. Sathe, R.J. Choudhary, P.K. Gupta, Strong magnetoelectric and spin phonon coupling in  $\text{SmFeO}_3/\text{PMN-PT}$  composite. *Appl. Phys. Lett.* **109**, 082902 (2016). <https://doi.org/10.1063/1.4961581>
- A. Ahlawat, S. Satapathy, P. Deshmukh, M.M. Shirolkar, A.K. Sinha, A.K. Karnal, Electric field poling induced self-biased converse magnetoelectric response in  $\text{PMN-PT}/\text{NiFe}_2\text{O}_4$  nanocomposites. *Appl. Phys. Lett.* **111**, 262902 (2017). <https://doi.org/10.1063/1.5008443>
- A. Ahlawat, A.A. Khan, P. Deshmukh, M.M. Shirolkar, S. Satapathy, R.J. Choudhary, D.M. Phase, Effect field

- controlled magnetization in NiFe<sub>2</sub>O<sub>4</sub>/SrRuO<sub>3</sub>/PMN-PT heterostructures for nonvolatile memory applications: XMCD study. *Appl. Phys. Lett.* **119**, 112902 (2021). <https://doi.org/10.1063/5.0061470>
14. S.E. Park, T.R. Shrout, Ultrahigh strain and piezoelectric behavior in relaxor based ferroelectric single crystals. *J. Appl. Phys.* **82**, 1804–1811 (1997). <https://doi.org/10.1063/1.365983>
  15. F.L. Zabotto, A.J. Gualdi, J.A. Eiras, A.J.A. de Oliveira, D. Garcia, Angular dependence of the magnetoelectric effect on PMN-PT/CFO particulate composites. *Integr. Ferroelectr.* **131**, 127–133 (2011). <https://doi.org/10.1080/10584587.2011.616428>
  16. D. Fritsch, C. Ederer, Epitaxial strain effects in the spinel ferrites CoFe<sub>2</sub>O<sub>4</sub> and NiFe<sub>2</sub>O<sub>4</sub> from first principles. *Phys. Rev. B* **82**, 104117 (2010). <https://doi.org/10.1103/PhysRevB.82.104117>
  17. B. Ghosh, M. Sardar, S. Banerjee, Effect of antisite formation on magnetic properties of nickel zinc ferrite particles. *J. Appl. Phys.* **114**, 183903 (2013). <https://doi.org/10.1063/1.4829704>
  18. A. Ahlawat, A. Ali Khan, P. Deshmukh, M.M. Shirolkar, J. Li, H. Wang, R.J. Choudhary, A.K. Karnal, S. Satapathy, Flexible nanocomposite films of CoFe<sub>2</sub>O<sub>4</sub>/(0.65Pb(Mg<sub>1/3</sub>Nb<sub>2/3</sub>)O<sub>3</sub>–0.35PbTiO<sub>3</sub>)/PMMA for non-volatile memory applications. *Mater. Lett.* **278**, 128425 (2020). <https://doi.org/10.1016/j.matlet.2020.128425>
  19. A. Ahlawat, V.G. Sathe, Raman study of NiFe<sub>2</sub>O<sub>4</sub> nanoparticles, bulk and films: effect of laser power. *J. Raman Spectrosc.* **42**, 1087–1094 (2011). <https://doi.org/10.1002/jrs.2791>
  20. P. Chandramohan, M.P. Srinivasan, S. Velmurugan, S.V. Narasimhan, Cation distribution and particle size effect on Raman spectrum of CoFe<sub>2</sub>O<sub>4</sub>. *J. Solid State Chem.* **184**, 89–96 (2011). <https://doi.org/10.1016/j.jssc.2010.10.019>
  21. A. Slodczyk, P. Daniel, A. Kania, Local phenomena of (1-x)PbMg<sub>1/3</sub>Nb<sub>2/3</sub>O<sub>3</sub>-xPbTiO<sub>3</sub> single crystals (0 < x < 0.38) studied by Raman scattering. *Phys. Rev. B* **77**, 184114 (2008). <https://doi.org/10.1103/PhysRevB.77.184114>
  22. B. Noheda, D.E. Cox, G. Shirane, J. Gao, Z.-G. Ye, Phase diagram of the ferroelectric relaxor 1-xPbMg<sub>1/3</sub>Nb<sub>2/3</sub>O<sub>3</sub>-xPbTiO<sub>3</sub>. *Phys. Rev. B* **66**, 54104 (2002). <https://doi.org/10.1103/PhysRevB.66.054104>
  23. H. Uršič, M. Hrovat, J. Holc, J. Tellier, S. Drnovšek, N. Guiblin, B. Dkhil, M. Kosec, Influence of the substrate on the phase composition and electrical properties of 0.65PMN–0.35PT thick films. *J. Eur. Ceram. Soc.* **30**, 2081–2092 (2010). <https://doi.org/10.1016/j.jeurceramsoc.2010.04.010>
  24. V. Šepelák, A. Buchal, K. Tkáčová, K.D. Becker, Nanocrystalline structure of the metastable ball-milled inverse spinel-ferrites. *Mater. Sci. Forum.* **278–281**, 862–867 (1998). <https://doi.org/10.4028/www.scientific.net/MSF.278-281.862>
  25. A. Franco Jr., H.V.S. Pessoni, F.O. Neto Mossbauer, Enhanced high temperature magnetic properties of ZnO-CoFe<sub>2</sub>O<sub>4</sub> ceramic composite. *J. Alloy Compd* **680**, 198e205 (2016). <https://doi.org/10.1016/j.jallcom.2016.04.110>
  26. F.D. Saccone, S. Ferrari, D. Errandonea, F. Grinblat, V. Bilovol, S. Agouram, Cobalt ferrite nanoparticles under high pressure. *J. Appl. Phys.* **118**, 75903 (2015). <https://doi.org/10.1063/1.4928856>
  27. M.A. Laguna-Bercero, M.L. Sanjuán, R.I. Merino, Raman spectroscopic study of cation disorder in poly- and single crystals of the nickel aluminate spinel. *J. Phys. Condens. Matter.* **19**, 186217 (2007). <https://doi.org/10.1088/0953-8984/19/18/186217>
  28. E. Granado, A. Garcia, J.A. Sanjurjo, C. Rettori, I. Torriani, F. Prado, R.D. Sánchez, A. Caneiro, S.B. Oseroff, Magnetic ordering effects in the Raman spectra of La<sub>1-x</sub>Mn<sub>1-x</sub>O<sub>3</sub>. *Phys. Rev. B.* **60**, 11879–11882 (1999). <https://doi.org/10.1103/PhysRevB.60.11879>
  29. M. Balkanski, R.F. Wallis, E. Haro, Anharmonic effects in light scattering due to optical phonons in silicon. *Phys. Rev. B.* **28**, 1928–1934 (1983). <https://doi.org/10.1103/PhysRevB.28.1928>
  30. Y.Y. Zhao, J. Wang, H. Kuang, F.-X. Hu, Y. Liu, R.-R. Wu, X.-X. Zhang, J.-R. Sun, B.-G. Shen, Anisotropic modulation of magnetic properties and the memory effect in a wide-band (011)-Pr<sub>0.7</sub>Sr<sub>0.3</sub>MnO<sub>3</sub>/PMN-PT heterostructure. *Sci. Rep.* **5**, 9668 (2015). <https://doi.org/10.1038/srep09668>
  31. G.H. Jaffari, A.K. Rumaiz, J.C. Woicik, S.I. Shah, Influence of oxygen vacancies on the electronic structure and magnetic properties of NiFe<sub>2</sub>O<sub>4</sub> thin films. *J. Appl. Phys.* **111**, 093906 (2012). <https://doi.org/10.1063/1.4704690>
  32. S. Ayyappan, S.P. Raja, C. Venkateswaran, J. Philip, B. Raj, Room temperature ferromagnetism in vacuum annealed ZnFe<sub>2</sub>O<sub>4</sub> nanoparticles. *Appl. Phys. Lett.* **96**, 143106 (2010). <https://doi.org/10.1063/1.3374332>
  33. E. Pellegrin, M. Hagelstein, S. Doyle, H.O. Moser, J. Fuchs, D. Vollath, S. Schuppler, M.A. James, S.S. Saxena, L. Niesen, O. Rogojuanu, G.A. Sawatzky, C. Ferrero, M. Borowski, O. Tjernberg, N.B. Brookes, Characterization of nanocrystalline γ-Fe<sub>2</sub>O<sub>3</sub> with synchrotron radiation techniques. *Phys. Status Solidi.* **215**, 797–801 (1999). [https://doi.org/10.1002/\(SICI\)1521-3951\(199909\)215:1%3c797::AID-PSSB797%3e3.0.CO;2-D](https://doi.org/10.1002/(SICI)1521-3951(199909)215:1%3c797::AID-PSSB797%3e3.0.CO;2-D)
  34. R.A.D. Patrick, G. Van Der Laan, C.M.B. Henderson, P. Kuiper, E. Dudzik, D.J. Vaughan, Cation site occupancy in spinel ferrites studied by X-ray magnetic circular dichroism: developing a method for mineralogists. *Eur. J. Mineral.* **14**, 1095–1102 (2002). <https://doi.org/10.1127/0935-1221/2002/0014-1095>

35. H.B. Vasili, M. Gamino, J. Gázquez, F. Sánchez, M. Valvidares, P. Gargiani, E. Pellegrin, J. Fontcuberta, Magnetoresistance in hybrid Pt/CoFe<sub>2</sub>O<sub>4</sub> bilayers controlled by competing spin accumulation and interfacial chemical reconstruction. *ACS Appl. Mater. Interfaces* **10**, 12031–12041 (2018). <https://doi.org/10.1021/acsami.8b00384>
36. E. Stavitski, F.M.F. de Groot, The CTM4XAS program for EELS and XAS spectral shape analysis of transition metal L edges. *Micron* **41**, 687–694 (2010). <https://doi.org/10.1016/j.micron.2010.06.005>
37. B.T. Thole, P. Carra, F. Sette, G. van der Laan, X-ray circular dichroism as a probe of orbital magnetization. *Phys. Rev. Lett.* **68**, 1943–1946 (1992). <https://doi.org/10.1103/PhysRevLett.68.1943>
38. C.T. Chen, Y.U. Idzerda, H.-J. Lin, N.V. Smith, G. Meigs, E. Chaban, G.H. Ho, E. Pellegrin, F. Sette, Experimental confirmation of the X-ray magnetic circular dichroism sum rules for iron and cobalt. *Phys. Rev. Lett.* **75**, 152–155 (1995). <https://doi.org/10.1103/PhysRevLett.75.152>
39. D.M. Phase, G. Panchal, R. Rawat, S. Tiwari, R. Prakash, D. Jain, R.J. Choudhary, Anomalous magnetic properties of Fe<sub>3</sub>O<sub>4</sub> nanostructures on GaAs substrate probed using X-ray magnetic circular dichroism. *J. Magn. Magn. Mater.* **482**, 296–300 (2019). <https://doi.org/10.1016/j.jmmm.2019.03.041>
40. Y. Zhou, S. Chul Yang, D.J. Apo, D. Maurya, S. Priya, Tunable self-biased magnetoelectric response in homogenous laminates. *Appl. Phys. Lett.* **101**, 232905 (2012). <https://doi.org/10.1063/1.4769365>
41. T. Walther, U. Straube, R. Köferstein, S.G. Ebbinghaus, Hysteretic magnetoelectric behavior of CoFe<sub>2</sub>O<sub>4</sub>–BaTiO<sub>3</sub> composites prepared by reductive sintering and reoxidation. *J. Mater. Chem. C* **4**, 4792–4799 (2016). <https://doi.org/10.1039/C6TC00995F>
42. S. Chul Yang, K.-H. Cho, C.-S. Park, S. Priya, Self-biased converse magnetoelectric effect. *Appl. Phys. Lett.* **99**, 202904 (2011). <https://doi.org/10.1063/1.3662420>

**Publisher's Note** Springer Nature remains neutral with regard to jurisdictional claims in published maps and institutional affiliations.

Springer Nature or its licensor holds exclusive rights to this article under a publishing agreement with the author(s) or other rightsholder(s); author self-archiving of the accepted manuscript version of this article is solely governed by the terms of such publishing agreement and applicable law.